Supporting Information

Dually Encapsulated $LiMn_{0.6}Fe_{0.4}PO_4$ Architecture with MXene and Amorphous Carbon to Achieve High-performance and Ultra-stable Lithium Battery

Yang Song[a], Haidong Zhong[a], Tingting Hu[a], Qizhi Chen[c], Lei Shi[c], Jun Du[a],

Changyuan Tao[a,b,], Qian Zhang[a,*]*

[a]School of Chemistry and Chemical Engineering, Chongqing University, Chongqing 400044, China

[b]State Key Laboratory of Coal Mine Disaster Dynamics and Control, Chongqing University, Chongqing, 400044, China

[c]Guangxi Huiyuan Manganese Industry Co., Ltd. Laibin City, Guangxi, 546138, China

*Corresponding Author E-mail: taocy@cqu.edu.cn (Changyuan Tao)

*Corresponding Author E-mail: qianz@cqu.edu.cn (Qian Zhang)

S1 Synthesis and materials characterization

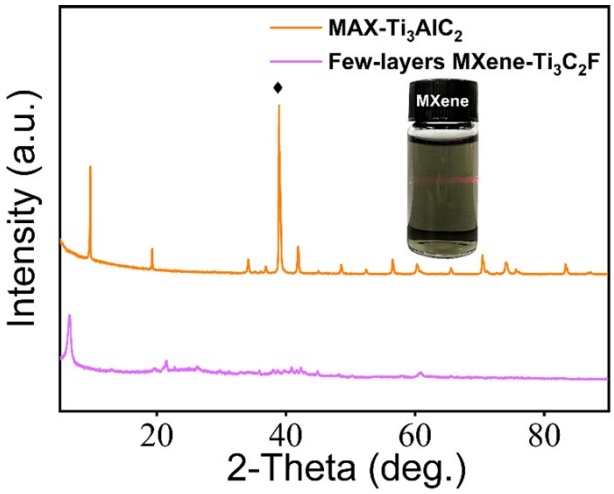

Figure S1. XRD patterns of Ti_3AlC_2 and few-layers MXene, as well as dispersion of few-layers MXene.

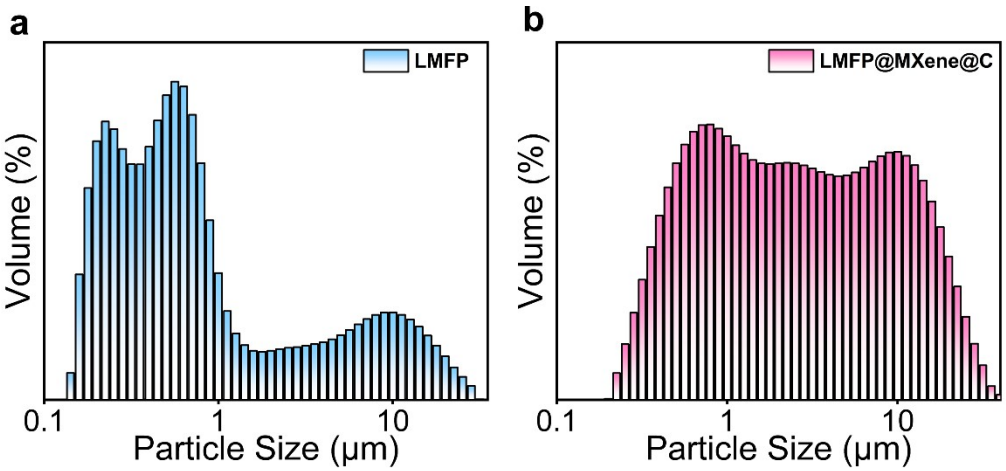

Figure S2. Particle size distribution of LMFP and LMFP@MXene@C.

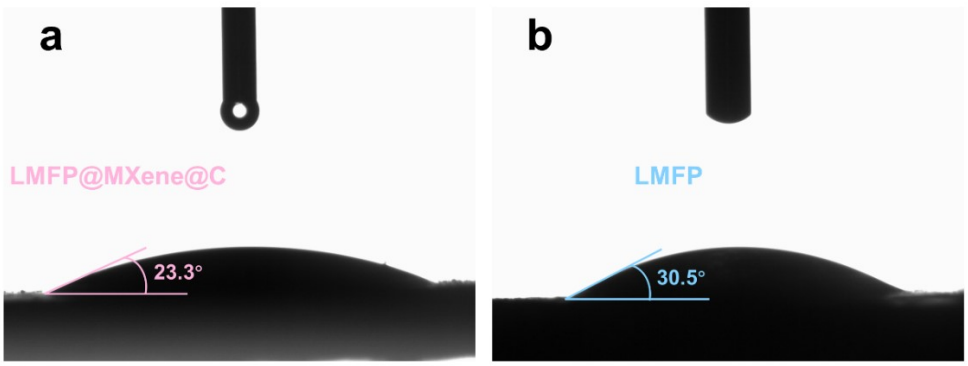

Figure S3. The wetting angles of LMFP@MXene@C and LMFP with the electrolyte, respectively.

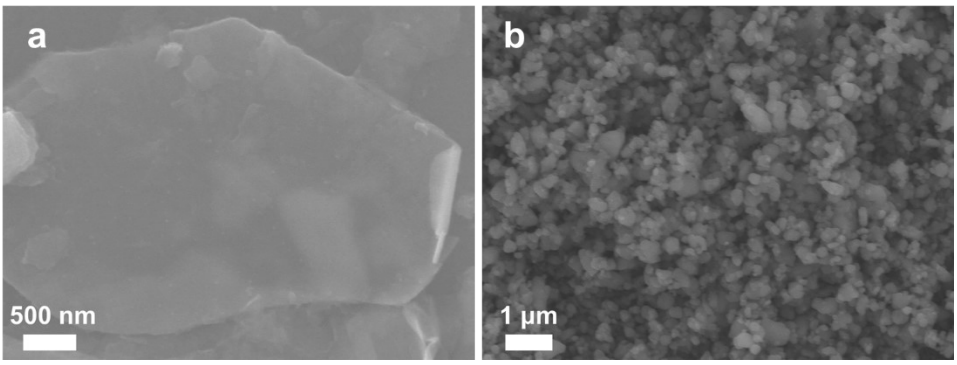

Figure S4. SEM of few-layers MXene and LMFP.

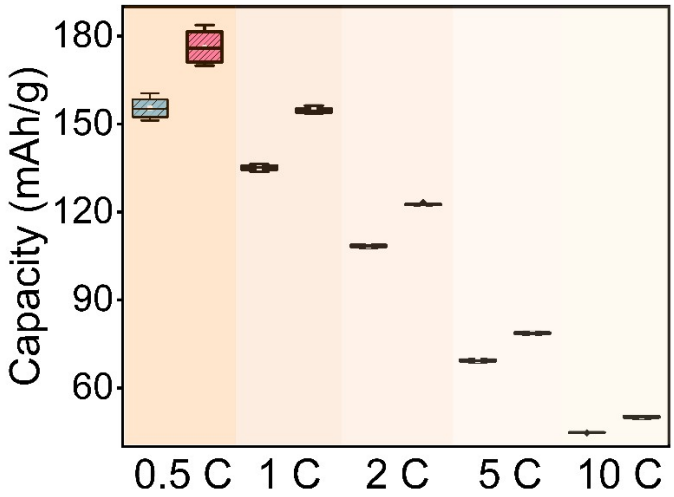

Figure S5. Box diagram of rate performance of the LMFP@MXene@C and LMFP cathodes.

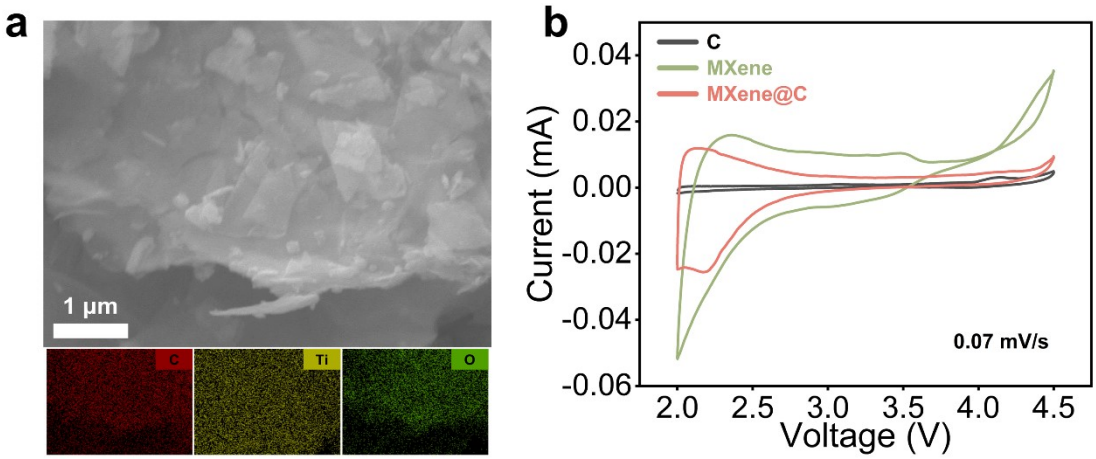

Figure S6. (a) SEM and mapping of MXene@C. (b) CV of pure C (derived citric acid), MXene and MXene@C.

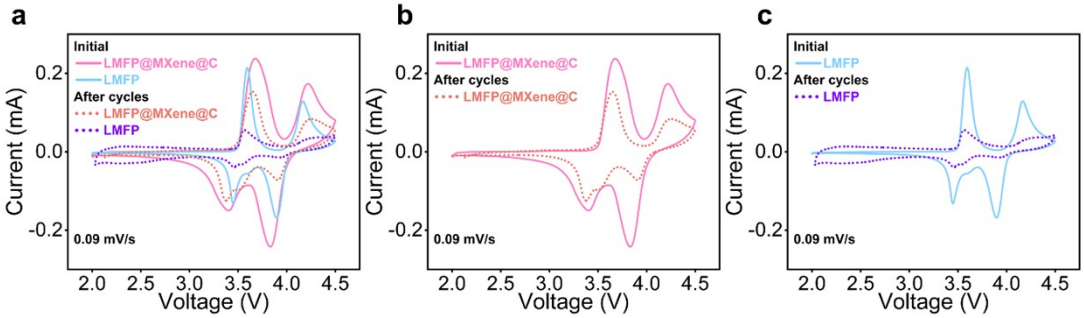

Figure S7. a-c shows the CV comparison between LMFP@MXene@C and LMFP at the beginning and after cycling for 1200 under 5C.

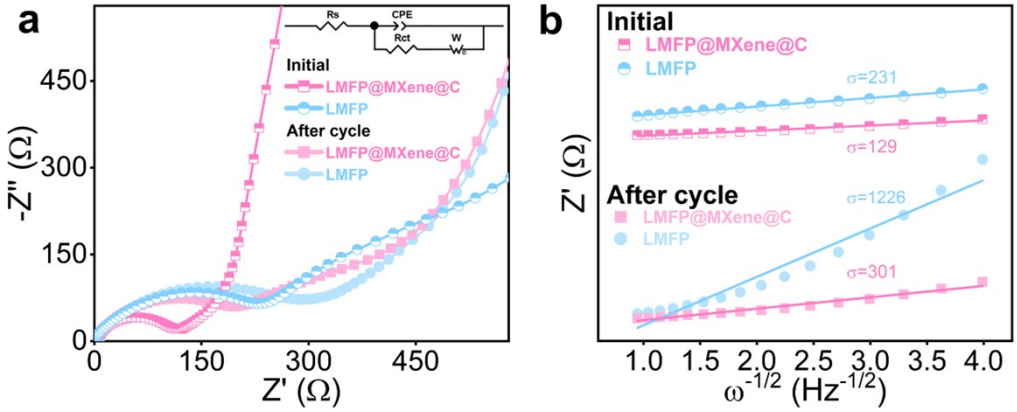

Figure S8. EIS spectra and Nyquist plots, and relationship between Z' and $\omega^{-1/2}$ at low frequencies of LMFP and LMFP@MXene@C initially and after long cycles.

S2 Electrochemical performance and ion diffusion kinetics

Typically, the voltage range was set as 2-4.5 V, and the GITT tests were carried out at 0.5 C with a pulse of 30 min and a relaxation of 30 min. The calculation of the diffusion coefficient was based on the following equation:

$$D = \frac{4l^2}{\pi\tau}\left(\frac{\triangle E_s}{\triangle E_t}\right)$$

where D represents the ion diffusion coefficient, l is the thickness of the active materials, and τ is the relaxation time. ΔE_s refers to the voltage difference between the voltages before the pulse process and after relaxing. ΔE_t is the voltage variation eliminating the IR drop during pulse.

The charge-storage mechanism can be investigated by exploring the relationship between the peak current (i, mA) and the scan rates (v, mV s^{-1}) by Eq.(1)-(2):

$$i = av^b$$

$$\log(i) = b\log(v) + \log(a)$$

Where a and b are adjustable parameters. When b equals to 1, the capacity is fully governed by the capacitive-controlled process; if b equals to 0.5, it corresponds to a diffus ion-controlled process.[13, 14]

The respective contribution of capacitive-controlled processes and diffusion-controlled process can be quantitatively estimated through the following Eq.(3)-(4):

$$i(v) = k_1 v + k_2 v^{1/2}$$

$$i(v)/v^{1/2} = k_1 v^{1/2} + k_2$$

Where $i(v)$, $k_1 v$, $k_2 v^{1/2}$ and v refer to the current at a fixed potential, the capacitive-controlled current, the diffusion-controlled current and the scan rate, respectively.[15, 16]

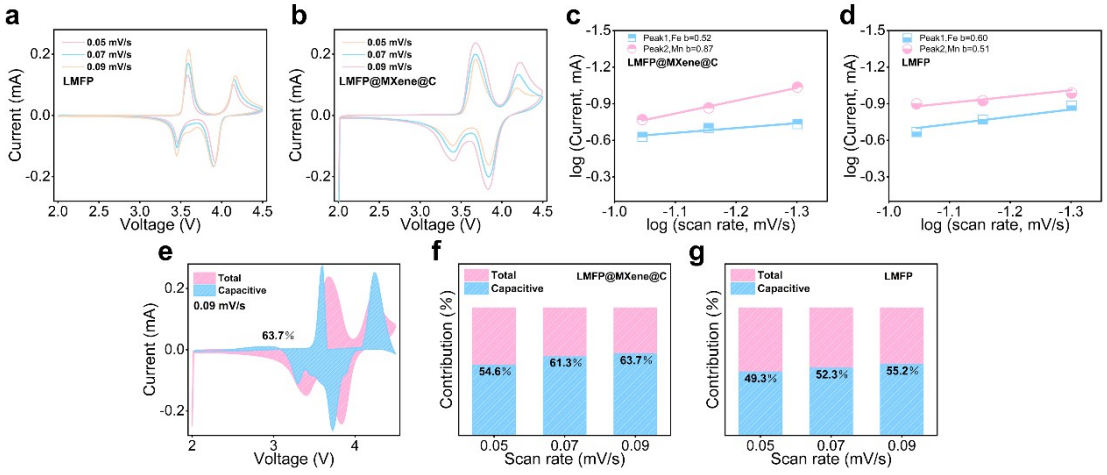

Figure S9. (a)-(b) CV curves of LMFP@MXene@C and LMFP cathode at various scan rates; (c)-(d) log*(i)* vs log*(v)* plot of LMFP@MXene@C and LMFP; (e) diffusion and capacitive contributions of the LMFP@MXene@C at 0.09 mV s^{-1}; (e)-(g) capacitive contribution of the LMFP@MXene@C and LMFP at various scan rates.

S4 Evaluation of electrode materials stabilities

The International Conference on Thermal Analysis and Calorimetry indicates that a reliable thermodynamic model should be based on data obtained under multiple β

values. In addition, the equal conversion method should be used to calculate the reaction kinetics. Therefore, in order to study the thermal stability of cathode materials, based on thermodynamic data obtained from DSC, we used Starink, Vyazovkin, KAS and FWO models to calculate E_a at different heating rates s (β = 1, 2, 4, 7, and 10 ◦C/min). Thus, mutual authentication was achieved based on the accuracy of E_a values.[17]

The thermokinetic parameters of the Starink model are calculated using Eq. (1):

$$\ln\left(\frac{\beta}{T_p^i}\right) = C_s - C\left(\frac{E_a}{RT}\right)$$

where C_s is the constant and i and C are approximate values of the temperature integral. In this study, i and C were specified as 1.80 and 1.0037, respectively.

The thermokinetic parameters of the Vyazovkin model are calculated using Eq. (2):

$$-\ln t_{\alpha,t} = \ln\left[\frac{A}{G(\alpha)}\right] - \frac{E_a}{RT}$$

where $t_{\alpha,t}$ represents the time required for the electrode material to achieve different thermal conversion rates.

The thermokinetic parameters of the KAS model are calculated by Eq. (3):

$$\ln\left(\frac{\beta}{T_\alpha^2}\right) = \ln\left[\frac{AR}{E_a G(\alpha)}\right] - \frac{E_a}{RT_\alpha}$$

where g(α) is an integral form of the reaction mechanism function and T_α is the temperature corresponding to the conversion rate α. In order to set a baseline when analyzing the data, we randomly selected 12 conversion degrees (α= 0.05, 0.1, 0.2, 0.3, 0.4, 0.5, 0.6, 0.7, 0.8, 0.9, 0.95, and 0.99) are used for thermodynamic analysis.[18]

The Flynn-Wall-Ozawa (FWO) kinetic model inherits the advantages of the differential and isoconversional models. The FWO kinetic model is used as a representative integral method and compared with the Kissinger, KAS, and Vyazovkin kinetic models. The thermokinetic parameters of the FWO model are calculated using Eq. (4):

$$In(\beta_1) + 1.0516\left(\frac{E_a}{RT_{p1}}\right) = In(\beta_2) + 1.0516\left(\frac{E_a}{RT_{p2}}\right) = In(\beta_3) + 1.0516\left(\frac{E_a}{RT_{p3}}\right) = \ldots$$

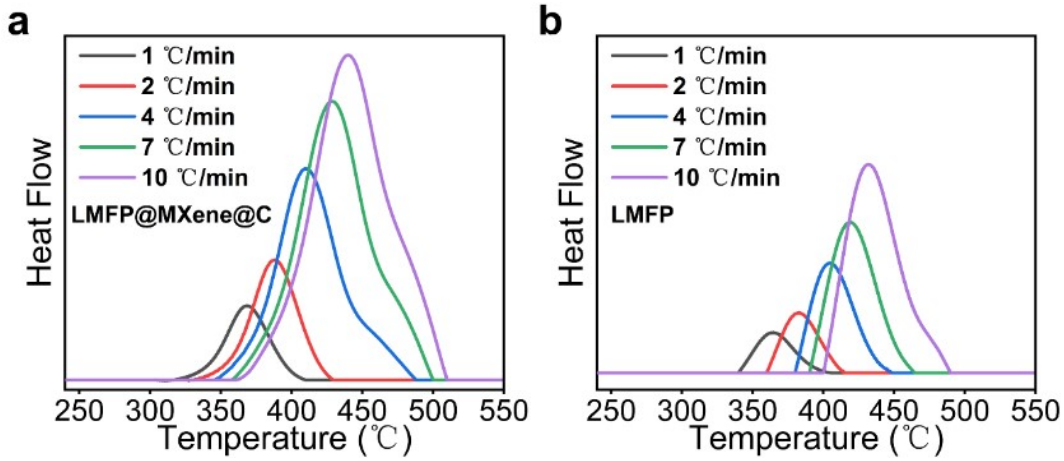

Figure S10. Heat absorption curves of LMFP@MXene@C and LMFP at different heating rates.

Table S1. The composition and analysis method of commercial LMFP.

	%	Test method
Li	4.3	ICP standard curve method
Mn	20.65	
Fe	13.88	
P	19.21	
C	1.87	carbon sulfur analyzer

Table S2. Performance of LMFP analogue materials reported in literatures.

Phase information	Performance	References
$LiMn_{0.5}Fe_{0.5}PO_4$@(rGo+C)	115 mAh g^{-1} at 1 C	[1] J. Power Sources 329 (2016) 94–103
C-$LiMn_{0.8}Fe_{0.2}PO_4$	~145 mAh g^{-1} at 1 C	[2] Electrochim. Acta 191 (2016) 200-206
$LiMn_{0.8}Fe_{0.2}PO_4$/C/N-rGo	135.4 mAh g^{-1} at 1 C	[3] Appl. Surf. Sci. 476 (2019) 513-520
$LiFe_{0.6}Mn_{0.4}PO_4$/C with FACP	150.8 mAh g^{-1} at 1 C	[4] J. Power Sources 275 (2015) 823-830
Porous $LiFe_{0.4}Mn_{0.6}PO_4$/CNFs	138.8 mAh g^{-1} at 1 C	[5] Chem. Eur. J. 26 (2020) 5341 – 5346
LMFP/rGO@C	152 mAh g^{-1} at 1C	[6] Appl. Energy Mater. 2 (2019) 2 1727−1733
$LiFe_{0.8}Mn_{0.2}PO_4$-3S3C2P composites	130 mAh g^{-1} at 1 C	[7] J. Mater. Chem. A 6 (2018) 10395–10403
$LiFe_{0.4}Mn_{0.6}PO_4$-1LZO	< 130 mAh g^{-1} at 1 C	[8] J. Power Sources 613 (2024) 234938
$Li_4Ti_5O_{12}$ Coated $LiMn_{0.6}Fe_{0.4}PO_4$	140.5 mAh g^{-1} at 1 C	[9] J. Electrochem. Soc. 171 (2024) 040502
Mg-doped $LiMn_{0.8}Fe_{0.2}PO_4$/C	145.8 mAh g^{-1} at 1 C	[10] J. Energy Storage 73 (2023) 109006
$LiMn_{0.5}Fe_{0.5}PO_4$-Zn (1%)	128.7 mAh g^{-1} at 1 C	[11] J. Energy Storage 96 (2024) 112552
LMFP/C-Fe	152.4 mAh g^{-1} at 1 C	[12] J. Energy Storage 79 (2024) 110198
$LiMn_{0.6}Fe_{0.4}PO_4$@MXene@C	154 mAh g^{-1} at 1 C	This work

LMFP and LMFP@MXene@C's GITT corresponding data under accession code https://doi.org/10.6084/m9.figshare.26942950.

Table S3. The charge transfer impedance, weber factor and diffusion coefficient of samples.

Samples	R_{ct}/Ω	σ/ohm$cm^2s^{-0.5}$	D_{Li+}/cm^2s^{-1}
LMFP	249.7	231	1.64337×10^{-13}
LMFP@MXene@C	114.8	129	5.26961×10^{-13}
Cycles-LMFP	301.7	1226	5.83415×10^{-15}

Cycles-LMFP@MXene@C	211.7	301	9.67888×10^{-14}

Table S4. E_a and R^2 values calculation for the cathode material of LMFP@MXene@C using three models under different α values.

α	Starink		Vyazovkin		KAS		FWO	
	E_a (kJ/mol)	R^2	E_a (kJ/mol)	R^2	E_a (kJ/mol)	R^2	E_a (kJ/mol)	R^2
10	125.49	0.998	125.69	0.99	124.88	0.99	129.01	0.99
20	118.88	0.99	119.17	0.99	118.22	0.99	122.84	0.99
30	113.79	0.998	114.13	0.99	113.11	0.99	118.07	0.99
40	110.26	0.99	110.66	0.99	109.55	0.99	114.78	0.99
50	106.86	0.99	107.31	0.99	106.13	0.99	111.61	0.99
60	104.16	0.99	104.66	0.99	103.41	0.99	109.11	0.99
70	99.21	0.99	99.75	0.99	98.43	0.99	104.46	0.99
80	93.80	0.99	94.41	0.99	92.99	0.99	99.40	0.99
90	86.27	0.98	86.96	0.98	85.42	0.98	92.35	0.98
95	82.07	0.96	82.82	0.96	81.19	0.96	88.45	0.97
Average	104.08	0.99	104.56	0.99	103.33	0.99	109.01	0.99

Table S5. E_a and R^2 values calculation for the cathode material of LMFP using three models under different α values.

α	Starink		Vyazovkin		KAS		FWO	
	E_a (kJ/mol)	R^2	E_a (kJ/mol)	R^2	E_a (kJ/mol)	R^2	E_a (kJ/mol)	R^2
10	113.79	0.99	113.89	0.99	113.13	0.99	117.79	0.99
20	109.73	0.99	109.93	0.99	109.05	0.99	114.05	0.99
30	106.59	0.99	106.86	0.99	105.89	0.99	111.15	0.99
40	103.38	0.99	103.71	0.99	102.65	0.99	108.16	0.99
50	100.07	0.99	100.45	0.99	99.32	0.99	105.08	0.99
60	95.35	0.99	95.79	0.99	94.58	0.995	100.67	0.99
70	88.95	0.99	89.45	0.99	88.14	0.99	94.66	0.99
80	81.46	0.98	82.04	0.99	80.61	0.98	87.65	0.99
90	72.76	0.98	73.44	0.98	71.85	0.97	79.51	0.98
95	67.87	0.97	68.64	0.97	66.93	0.97	74.98	0.97
Average	94.00	0.99	94.42	0.99	93.22	0.99	99.37	0.99

REFERENCES

[1] Wei, X.; Zhen-Guo, W.; En-Hui, W.; Ming-Zhe, C.; Yang, S.; Ji-Bin, Z., Confined synthesis of graphene wrapped $LiMn_{0.5}Fe_{0.5}PO_4$ composite via two step solution phase method as high performance cathode for Li-ion batteries, Journal of Power Sources 329 (2016), 94-103.

[2] Liangtao, Y.; Yonggao, X.; Xu, F.; Laifen, Q.; Bao, Q.; Zhaoping, L., Constructing durable carbon layer on $LiMn_{0.8}Fe_{0.2}PO_4$ with superior long-term cycling performance for lithium-ion

battery, Electrochimica Acta 191 (2016), 200-206.

[3] Longquan, G.; Li, R.; Liu, W.; Jiashen, L., Heterogeneous carbon/N-doped reduced graphene oxide wrapping $LiMn_{0.8}Fe_{0.2}PO_4$ composite for higher performance of lithium ion batteries, Applied Surface Science 15 (2019), 513-520.

[4] Xinhe, Y.; Yingying, M.; Weidong, Z.; Borong, W.; Henghui, Z., Enhanced electrochemical performance of $LiFe_{0.6}Mn_{0.4}PO_4$/C cathode material prepared by ferrocene-assisted calcination process, Journal of Power Sources 275 (2015), 823-830.

[5] Jing, Y.; Rou, T.; Di, L.; Jianmin, M.; Xiaochuan, D., Ionic liquid assisted electrospinning of porous $LiFe_{0.4}Mn_{0.6}PO_4$/CNFs as free-standing cathodes with a pseudocapacitive contribution for high-performance lithium-ion batteries, Chemistry-A European Journal 26 (2020), 5341-5346.

[6] Dong, D.; Yuta, M.; Makasugi, k.; Jungo, W.; Kiyoshi, K., A facile way to synthesize carbon-coated $LiMn_{0.7}Fe_{0.3}PO_4$/reduced graphene oxide sandwich-structured composite for lithium-ion batteries, ACS Appied Energy Materials 2 (2019), 1727-1733.

[7] Yan, W.; Cheng-Yu, W.; Hao, Y.; Jenq-Gong, D., Rational design of a synthetic strategy, carburizing approach and pore-forming pattern to unlock the cycle reversibility and rate capability of micro-agglomerated $LiMn_{0.8}Fe_{0.2}PO_4$ cathode materials, Journal of Materials Chemistry A 6 (2018), 10395-10403.

[8] Yite, L.; Ying, S.; Xue, W.; Tao, H.; Aishui, Y., Li_2ZrO_3 coated $LiFe_{0.4}Mn_{0.6}PO_4$/C with enhanced cycling performance at elevated temperature for lithium-ion batteries, Journal of Power Sources 613 (2024), 234938.

[9] Haoyan, G.; Weida, L.; Quanchen, L.; Xinran, Li.; Hao, Y.; Quanjun, F., Electrochemical properties of $Li_4Ti_5O_{12}$ coated $LiMn_{0.6}Fe_{0.4}PO_4$ prepared by rheological phase reaction method, Journal of The Electrochemical Society 171 (2024), 040502.

[10] Hui, H.; Heng, L.; Yu, L.; Jiali, L.; Xiaolin, L.; Ruijuan, W., Mg-doped $LiMn_{0.8}Fe_{0.2}PO_4$/C nano-plate as a high-performance cathode material for lithium-ion batteries, Journal of Energy Storage 73 (2023), 109006.

[11] Byeong, J., J.; Jae, Y., S.; Feng, J.; Soon, P., J.; Chang, W., L., Providing high stability to suppress metal dissolution in $LiMn_{0.5}Fe_{0.5}PO_4$ cathode materials by Zn doping, Journal of Energy Storage 96 (2024), 112552.

[12] Hui, H.; Xiaolin, L.; Yu, L.; Jiarui, C.; Lei, W.; Zhi, L., Enhancing the ultra-high rate capability of manganese-based olivine cathode by in situ catalytic growth of graphene carbon layer, Journal of Energy Storage 79 (2024), 110198.

[13] Huang, J.; Tang, X.; Liu, K.; Fang, G.; He, Z.; Li, Z., Interfacial chemical binding and improved kinetics assisting stable aqueous Zn–MnO_2 batteries, Materials Today Energy 17 (2020), 100475.

[14] Li, X.; Ji, C.; Shen, J.; Feng, J.; Mi, H.; Xu, Y.; Guo, F.; Yan, X., Amorphous heterostructure derived from divalent manganese borate for ultrastable and ultrafast aqueous zinc ion storage, Advanced Science 10 (2023), 2205794.

[15] Liu, W.; Su, Q.; Zhu, R.; Shi, W.; Zhang, F.; Du, G.; Zhao, W.; Zhang, M.; Xu, B., Chemical lithiation-induced oxygen vacancies in MnO_2 at room temperature for aqueous zinc-ion batteries, ACS Applied Energy Materials 6 (2023), 6689-6699.

[16] Chen, Q.; Lou, X.; Yuan, Y.; You, K.; Li, C.; Jiang, C.; Zeng, Y.; Zhou, S.; Zhang, J.; Hou, G.; et al., Surface adsorption and proton chemistry of ultr-stabilized aqueous zinc–manganese

dioxide batteries, Advanced Materials 35 (2023), 2306294.

[17] Zhang, C.-Z.; Jiang, J.-C.; Huang, A.-C.; Tang, Y.; Xie, L.-J.; Zhai, J.; Xing, Z.-X., A novel multifunctional additive strategy improves the cycling stability and thermal stability of SiO/C anode Li-ion batteries, Process Safety and Environmental Protection 164 (2022), 555-565.

[18] Wu, Z.-H.; Wu, Y.; Tang, Y.; Jiang, J.-C.; Huang, A.-C., Evaluation of composite flame-retardant electrolyte additives improvement on the safety performance of lithium-ion batteries, Process Safety and Environmental Protection 169 (2023), 285-292.